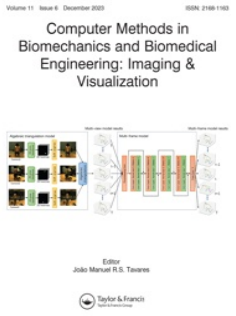

Taylor & Francis
Taylor & Francis Group

Computer Methods in Biomechanics and Biomedical Engineering: Imaging & Visualization

ISSN: (Print) (Online) Journal homepage: www.tandfonline.com/journals/tciv20

Accuracy of an articulated head-and-neck motion model using deep learning-based instance segmentation of skeletal bones in CT scans for image registration in radiotherapy

Alexandra Walter, Cornelius J. Bauer, Ama Katseena Yawson, Philipp Hoegen-Saßmannshausen, Sebastian Adeberg, Jürgen Debus, Oliver Jäkel, Martin Frank & Kristina Giske

To cite this article: Alexandra Walter, Cornelius J. Bauer, Ama Katseena Yawson, Philipp Hoegen-Saßmannshausen, Sebastian Adeberg, Jürgen Debus, Oliver Jäkel, Martin Frank & Kristina Giske (2025) Accuracy of an articulated head-and-neck motion model using deep learning-based instance segmentation of skeletal bones in CT scans for image registration in radiotherapy, Computer Methods in Biomechanics and Biomedical Engineering: Imaging & Visualization, 13:1, 2455752, DOI: 10.1080/21681163.2025.2455752

To link to this article: https://doi.org/10.1080/21681163.2025.2455752

COMPUTER METHODS IN BIOMECHANICS AND BIOMEDICAL ENGINEERING: IMAGING & VISUALIZATION
2025, VOL. 13, NO. 1, 2455752
https://doi.org/10.1080/21681163.2025.2455752

Accuracy of an articulated head-and-neck motion model using deep learning-based instance segmentation of skeletal bones in CT scans for image registration in radiotherapy

Alexandra Walter[a,b,c*], Cornelius J. Bauer[a,b,d*], Ama Katseena Yawson[a,b,e], Philipp Hoegen-Saßmannshausen[a,f,g], Sebastian Adeberg[h,i,j], Jürgen Debus[f,g,k], Oliver Jäkel[a,b,k], Martin Frank[c] and Kristina Giske[a,b]

[a]Division of Medical Physics in Radiation Oncology, German Cancer Research Center (DKFZ), Heidelberg, Germany; [b]Heidelberg Institute of Radiation Oncology (HIRO) & National Center for Radiation Research in Oncology (NCRO), Heidelberg/Dresden, Germany; [c]Scientific Computing Center, Karlsruhe Institute of Technology (KIT), Karlsruhe, Germany; [d]Faculty of Physics and Astronomy, University of Heidelberg, Heidelberg, Germany; [e]Faculty of Medicine, University of Heidelberg, Heidelberg, Germany; [f]Department of Radiation Oncology, Heidelberg University Hospital, Heidelberg, Germany; [g]Clinical Cooperation Unit Radiation Oncology, German Cancer Research Center (DKFZ), Heidelberg, Germany; [h]Department of Radiation Oncology, UKGM Marburg, Marburg, Germany; [i]Marburg Ion-Beam Therapy Center (MIT), Department of Radiation Oncology, UKGM Marburg, Marburg, Germany; [j]Universitäres Centrum für Tumorerkrankungen (UCT), Frankfurt - Marburg, Germany; [k]Heidelberg Ion Beam Therapy Center (HIT), Heidelberg University Hospital, Heidelberg, Germany

ABSTRACT

Knowing about anatomical deformations in patient images is crucial for adaptive image-guided radiation therapy. Biomechanical models ensure biofidelity in deformable image registration, but manual contouring limits their clinical use. We investigate the application of automatically generated contours for a biomechanical registration model in head and neck cancer treatment. For that, we automatically generate individual bone segmentations on planning CT scans examining a custom-trained nnU-Net model and the ready-trained TotalSegmentator model. Both sets of segmentations are evaluated using DICE, Hausdorff Distance and surface DICE. We investigate their impact on the build-up of the biomechanical articulated skeleton model by deviations in joint positioning and CT-CT registration accuracy using target registration error (TRE). The custom-trained model achieves 1.51 ± 0.26 mm TRE, with no significant difference in registration accuracy. While the TotalSegmentator does not provide all structures needed for the complete biomechanical model build-up. Overall, deep learning–based automatic bone segmentation can replace manual contouring in this model, matching its performance.

ARTICLE HISTORY
Received 6 September 2024
Accepted 14 January 2025

KEYWORDS
Biomechanical modelling; biofidelity; image registration; head and neck cancer; medical image segmentation

1. Introduction

Adaptive image-guided radiation therapy for cancer patients relies on image registration to assess motion and correct dosimetric consequences in the patient's body. To capture natural anatomical deformations, deformable image registration (DIR) is necessary. Intensity-based DIR algorithms are computationally efficient and easy to implement, but sensitive to image artefacts and experience issues optimising cases with large deformations (Kirby et al. 2011). Recently, deep learning–based DIR algorithms have been developed to predict deformation fields (Balakrishnan et al. 2015), though they still experience issues with large deformations, non-constrained registration and typically require large computational overhead when training (Zou et al. 2022). The lack of ground truth data can be an additional challenge as the correct transformation for real-world data is typically unknown (Fu et al. 2023).

In contrast, biomechanical models, offer accurate and biofidelic registration results (Brock et al. 2005; Bauer et al. 2023), but require segmentations of regions of interest (ROIs), a labour-intensive and slow process when done manually (Vaassen et al. 2020). Automatic segmentation generation has been extensively studied and remains an active area of research. For example, atlas-based segmentation, which registers a prior contoured reference image (the atlas) onto a new image, has sped up skeleton-based registration but has difficulties to represent the variation and details in skeleton anatomy (Yip et al. 2014).

Recently, deep learning–based image segmentation showed acceptable accuracy for many applications (Van Dijk et al. 2020). Although computationally demanding during training, deep learning methods offer adaptability and generalisation, handling artefacts and structure absence better than atlas-based methods. Artificial neural networks have successfully segmented individual bones, distinguishing instances of similar shape (Belal et al. 2019).

The variety of deep learning methods and datasets in the realm of medical image segmentation is vast (Campello et al. 2021, Liu et al. 2021,Magadza and Viriri 2021). Hyperparameter tuning is a demanding process, requiring significant time and resources due to the need for repeated model training (Arnold et al. 2023, Bergstra and Bengio 2012,

CONTACT Alexandra Walter Alexandra.walter@kit.edu Division of Medical Physics in Radiation Oncology, German Cancer Research Center (DKFZ), INF 280, 69120 Heidelberg, Germany

*These authors contributed equally to this work.

Supplemental data for this article can be accessed online at https://doi.org/10.1080/21681163.2025.2455752

Stergiopoulos et al. 2022). The nnU-Net framework (Isensee et al. 2021) is a self-configuring tool for medical image segmentation based on the U-Net architecture (Ronneberger et al. 2015), requiring no task-specific hyperparameter tuning. Based on this framework, the ready-trained open-access TotalSegmentator (TS) toolkit provides segmentation for 104 anatomical structures in the whole body, including multiple individual bones (Wasserthal et al. 2023).

In this study, we investigate the applicability and accuracy of deep learning–based bone segmentations for automating a biomechanically articulated skeleton registration model for application in head and neck cancer radiotherapy (Teske et al. 2017; Bauer et al. 2023). We trained a custom nnU-Net model and used the pre-trained TotalSegmentator framework to generate bone segmentations, analysing their capability for building up the articulated skeleton model and their impact on the biomechanical registration accuracy.

2. Material and methods

2.1. Data cohort

2.1.1. Image scans

This retrospective study included imaging data from 22 patients receiving curative radiotherapy between 1 January 2000, and 30 November 2022. Seventeen patients were treated in-house at the Heidelberg University Hospital (Stoiber et al. 2009, Stoiber et al. 2011, Stoiber et al. 2017) or at the clinical cooperation unit of the German Cancer Research Center (Giske et al. 2011), primarily for head and neck cancer or included same scanned body region. To increase the diversity of image features for training a deep-learning model, four imaging datasets from The Cancer Imaging Archive (Clark et al. 2013, Bejarano et al. 2018, Bosch et al. 2015) were added. These datasets, accessed on 1 November 2017, varied in device, protocol, treatment positioning, and patient age (Clark et al. 2013, Bejarano et al. 2018, Bosch et al. 2015, Zuley et al. 2016, Bejarano et al. 2019, Kiser et al. 2019, Ang et al. 2014). All scans were planning CTs of diagnostic quality, cropped to the necessary field of view for head and neck cancer treatment, including the skull base cranially and at least vertebra T3 caudally. Table A1 in the Appendix, summarises the source and specifications of the imaging data. No identifiable patient information was accessible to the authors.

Fourteen of these 22 datasets were used to train the custom nnU-Net model i.e. 7 in-house HNC patients, 2 open-access HNC datasets, 2 diagnostic scans with arms-up positioning, 2 in-house non-HNC patients, and one child anatomy. The test dataset contained the remaining 8 scans from the mentioned in-house cohorts. Three patients within the test dataset were accompanied by daily fraction CTs meeting the requirements for the biomechanical DIR model. In the following, these patients are referred to as fraction-patients i.e. patients 15–17 in Table A1. For each fraction-patient, 6 fraction CTs were used for the evaluation of the biomechanical DIR.

The CT scans had voxel sizes ranging from $0.98 \times 0.98 \times 2\ \mathrm{mm}^3$ to $1.37 \times 1.37 \times 3.3\ \mathrm{mm}^3$, with an in-plane matrix size of 512×512 and 97 to 198 slices. Voxels outside the semi-manually delineated patient skin were set to −1024. Study-specific patient consent was waived by ethics committee due to retrospective nature of the study. The ethics committee of the Medical Faculty of University Heidelberg approved the study under #S-660/2022.

2.1.2. Manual labels

For all CT scans, bones were manually delineated by different observers and refined by one observer. One scan was re-delineated by an independent observer to assess inter-observer variability. Figure 1 shows all contoured bones for a representative patient dataset. The standard operation procedure for delineation and refinement included: (a) Segmentation in the CT bone window (centre: 300 hU, width: 2000 hU), (b) synchronized 2D (5,3) Difference of Gaussians (DoG) filtered scans for visual guidance (centre: 0 hU, width: 100 hU), (c) skull and mandible contours excluding the teeth, (d) rib contours including the corresponding costal cartilages, (e) final shape refinements, especially edges of vertebral bodies, via sagittal view.

2.1.3. Pairs of landmarks for TRE

For the 3 patient datasets with daily fraction CTs (i.e. patient 15–17 in Table A1), a trained observer localised landmarks on the bones in the planning CT scans and six respective fraction CT scans (Bauer et al. 2023). Patient 15 had 161 landmarks, while patients 16 and 17 had 63–70 landmarks depending on visibility in the fraction CT scans.

The accuracy and robustness of the biomechanical DIR approach were evaluated quantitatively using corresponding pairs of landmarks on different (fraction) CT scans of the same patient. The evaluation was based on the target registration error (TRE), defined as the distance between corresponding landmarks (Maurer et al. 1993). Lower TRE indicates better local alignment of anatomical structures at the landmark position. In Bauer et al (2023), inter-observer variability for landmark identification ranged from 0.1 to 2.9 mm with a median of 1.1 mm (Bauer et al. 2023). This indicates the baseline of achievable landmark-based accuracy by a registration algorithm.

2.2. Automatically predicted labels

2.2.1. Generation and evaluation of predicted labels

The custom nnU-Net model was trained to predict 24 bone labels. The training used the nnU-Net's default hyperparameters and default preprocessing. Training and predictions were executed on a computer with an AMD Ryzen™ 9 3900X Processor, 128 GB RAM, a NVIDIA GeForce RTX 3090, and 24 GB VRAM. The TotalSegmentator Version 1 was originally trained on 1204 radiological CT scans from various sequences (Wasserthal et al. 2023) and was used as a Python library for prediction, on a computer with an Intel® Core™ i7 Processor, 64 GB RAM, a NVIDIA GeForce RTX 2070, and 8 GB VRAM. CT scans were split into three parts. Details about the training procedures, training parameters and network architecture are provided in the supplementary material.

The similarity of two different labels of the same structure was quantified by (a) their volumetric overlap using the Sørensen – Dice coefficient (DICE) (Dice 1945; Sørensen 1948), (b) their Hausdorff Distance (Rockafellar and Wets 2009), and (c) the proportion of the surfaces deviating more than 2 mm using

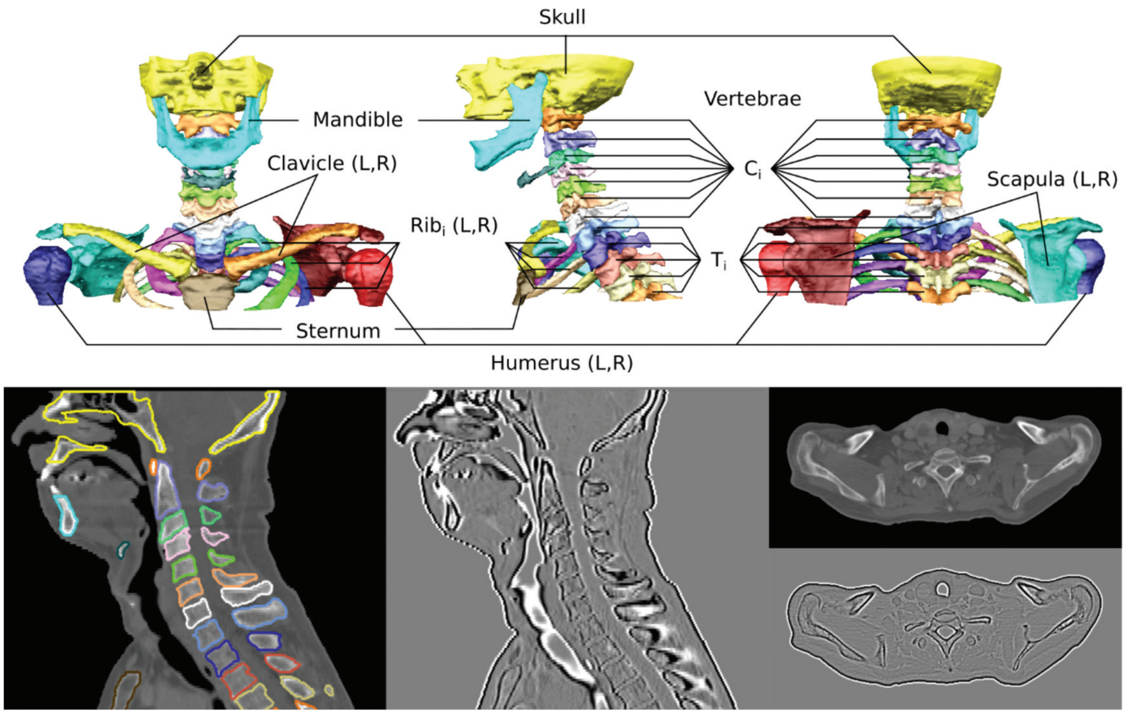

Figure 1. Visualization of the contouring data for a representative patient dataset from the training cohort. Upper row: rendering of the resulting individual bones required for the biomechanical model. Lower row: sagittal and transversal slices of the planning CT scan in bone window (300HU:2000HU) and the synchronized 2D (5,3) DoG filtered scan in the pre-defined window (0HU:100HU).

the surface DICE (sDICE) (Nikolov et al. 2021). Supported by the research of Wagenaar et al (2021) (Wagenaar et al. 2021), the threshold of 2 mm was chosen for the sDICE metric.

2.2.2. Post-processing of predicted labels

Post-processing the nnU-Net predictions, left and right instances of the clavicles, humeri, and scapulae were recombined, and a 3D volume grower was applied to separate the two largest connected components. All ribs were combined into a general rib label, with individual ribs extracted using connected components. Left and right rib instances were paired by comparing the cranio-caudal position of each centroid. No post-processing of the TotalSegmentator predictions was necessary.

The transformation of volume maps predicted by deep-learning models into contours necessary for the model build-up of the biomechanical model was performed with an in-house algorithm in VIRTUOS (Bendl 2006). Its integrity was verified by back-and-forth transformation between contours and volume maps.

2.3. Biomechanical DIR model and registration evaluation

The biomechanical DIR approach, previously published and applied to CT-CT registration with manual bone delineations (Bauer et al. 2023), uses an articulated biomechanical model build-up from individual bone segmentations to create a patient-specific static geometry. Joints are modelled as 3-degree-of-freedom ball-and-socket joints, positioned by nearest-neighbour or joint-specific rules (Teske et al. 2017, 2017). Inverse kinematics are solved using Simbody toolkit (Seth et al. 2010; Sherman et al. 2011), and bone positioning is optimised hierarchically using kinematic constraints and a Nelder-Mead-Simplex approach (Nelder and Mead 1965). Figure 2 shows the schematic approach of the biomechanical model registration including model build-up from the segmentations.

The accuracy of the joint positioning was measured as the Euclidean distance of the joint's centre point to the ground truth centre point acquired by the model build-up on the manual reference segmentations (Section 2.1.2). In the following, this metric is called the joint distance. Small values indicate consistent position of the joints.

The similarity metric that is optimised in the biomechanical DIR is calculated as the overlap of bones in the model and bones in the target image (areas above 120 hU in the CT). A displacement vector field (DVF) is generated for the full image space by applying motion propagation of the soft tissue via a modified chainmail deformation model and the skeletal input from the biomechanical model (Aguilera et al. 2015; Teske et al. 2017). This approach provides accurate and robust image registration comparable to standard intensity-based DIR algorithms while ensuring bone rigidity and articulation in the DVF (Bauer et al. 2023).

3. Results

3.1. Evaluation results of segmentations

3.1.1. Analysis of the generated labels

The TotalSegmentator lacks some critical labels, including the skull, mandible, hyoid bone, and sternum, which are necessary for building the biomechanical model. Additionally, the TotalSegmentator version 1 has systematic omissions, such as

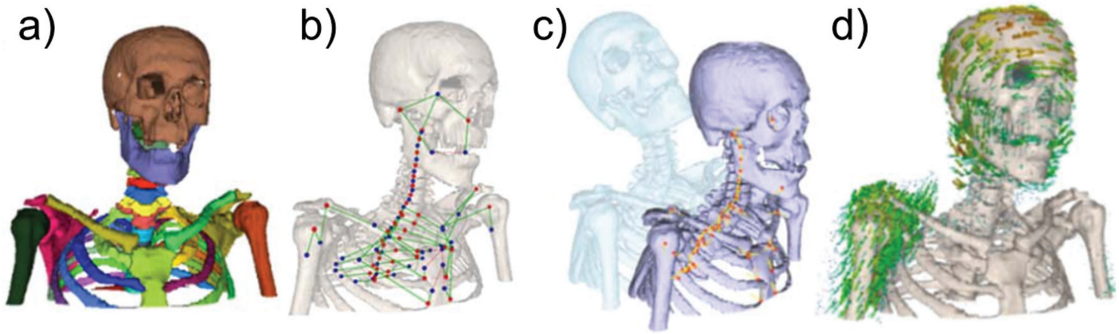

Figure 2. Representation of the biomechanical model (a) static skeleton geometry based on segmentations. (b) Build-up of the articulated biomechanical model by automatically positioning the involved joints (red points) and connections (green) of rigid bodies). (c) Model motion during optimization. (d) Resulting displacement vector field. Figure recreated from (Bauer et al. 2023).

missing cranial parts of the scapulae and sections of ribs at their junction with vertebrae, as shown in Figure 3. These omissions are consistently present in TotalSegmentator predictions and are detailed in (Wasserthal et al. 2023). Another deviation from our manual segmentation is the exclusion of costal cartilage, which is necessary for accurate costosternal joint positioning. Since the nnU-Net is trained on custom data, none of the aforementioned shortcomings holds for those predictions.

3.1.2. Comparison between manual labels and predictions

Table 1 shows the mean similarity metrics (DICE, HD, sDICE) for manual versus predicted labels from the custom-trained nnU-Net and the TotalSegmentator over all test patients, as well as DICE values found in the literature. Our custom nnU-Net generally shows better alignment with manual labels across all metrics. The nnU-Net's mean DICE, HD, and sDICE are 0.89 ± 0.05, 2.95 ± 1.97, and 0.95 ± 0.04, respectively, compared to the TS's 0.83 ± 0.08, 7.62 ± 7.43, and 0.91 ± 0.05. Significant improvements are seen with the nnU-Net for ribs and scapulae, with average gains of 0.09, 5.91, and 0.08 in DICE, HD, and sDICE. Except for an outlier in the right rib 1 caused by an error in post-processing, the variance in the mean DICE is low for all structures indicating consistent segmentation quality.

3.2. Evaluation of the biomechanical model and the biomechanical registration

3.2.1. Model build-up and joint positioning

The model build-up performance based on different segmentations is assessed by comparing distances of joint positioning. For patient 15, we evaluate the impact of inter-observer variability on joint positioning. Figure 4 shows the distances between the joints grouped into inter-vertebral joints, costosternal joints, costovertebral joints, and joints involving the scapula. Compared to manual labels, the nnU-Net and TotalSegmentator results show median joint distances of 2.6 mm and 2.2 mm for vertebral bodies, respectively, which is about 1 mm larger than the inter-observer variability (1.4 mm, blue boxplots in Figure 4).

For costosternal joints, nnU-Net achieves 4.0 mm compared to 19.2 mm with the TotalSegmentator and 5.5 mm inter-observer variability. Costovertebral joints results in 2.9 mm, 13.6 mm and 1.5 mm, respectively. Similarly, nnU-Net outperforms TotalSegmentator for scapulae-related joints with a median

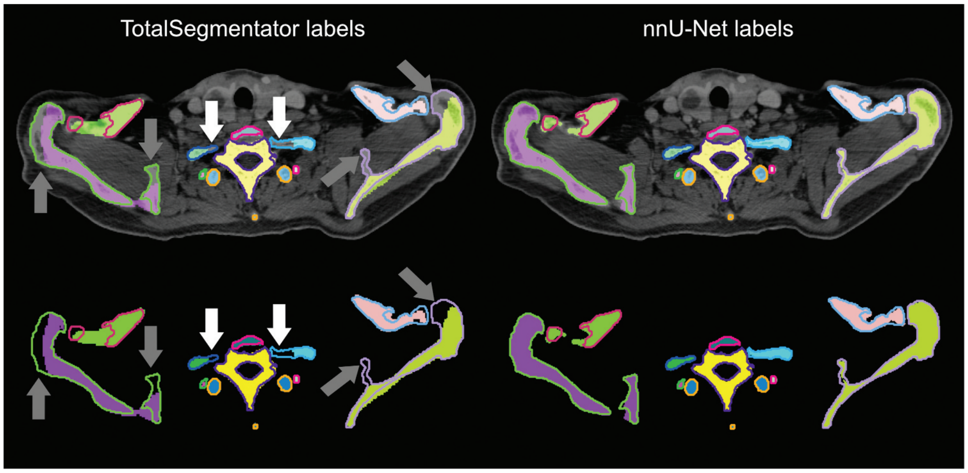

Figure 3. Comparison of manual labels (contours) and predicted labels (area) by the TotalSegmentator (left) and the custom trained nnU-net (right) on the CT scan (upper) and solely (lower). Pronounced deviations of the TotalSegmentator labels are between the ribs and the vertebra (white arrows) as well as in the segmentation of the scapulae (grey arrows). Different colors indicate different bones.

Table 1. The mean of the DICE, HD (95%) and sDICE with 2 mm tolerance between manual labels and the predictions of the nnU-Net and the TotalSegmentator over all 8 test patients. DICE values found in the literature are added in brackets.

	DICE		HD (95%) [mm]		sDICE (2 mm tol.)	
manual vs.	nnU-Net	TS	nnU-Net	TS	nnU-Net	TS
Skull	0.88	-	2.85	-	0.94	-
Mandible	0.91 (0.86–0.99) (Bendl 2006; Seth et al. 2010; Sherman et al. 2011; Teske et al. 2017; Vaassen et al. 2020)	-	4.39	-	0.96	-
Scapula (R)	0.93 (0.92) (Bendl 2006)	0.83	0.98	6.89	0.99	0.90
Scapula (L)	0.93 (0.92) (Bendl 2006)	0.82	0.98	10.91	0.99	0.89
Humerus (R)	0.98	0.92	0.86	12.96	0.99	0.90
Humerus (L)	0.97	0.91	0.98	6.40	0.99	0.92
Clavicle (R)	0.94	0.89	1.08	2.84	0.99	0.93
Clavicle (L)	0.94	0.91	1.03	1.82	0.99	0.97
Sternum	0.93 (0.83) (Yip et al. 2014)	-	1.54	-	0.98	-
Hyoid	0.83	-	4.21	-	0.95	-
C1	0.88	0.84	2.81	2.89	0.94	0.93
C2	0.90 (0.82) (Nelder and Mead 1965)	0.87	2.24	2.90	0.95	0.94
C3	0.88	0.83	2.60	3.26	0.94	0.91
C4	0.87	0.83	2.89	2.68	0.93	0.92
C5	0.83	0.83	3.82	3.32	0.91	0.92
C6	0.84	0.83	3.12	2.78	0.91	0.93
C7	0.88	0.85	2.62	2.77	0.93	0.93
T1	0.91 (0.84) (Nelder and Mead 1965)	0.89	2.00	2.41	0.96	0.95
Rib 1 (R)	0.73	0.66	8.91	16.17	0.80	0.80
Rib 1 (L)	0.86	0.66	5.37	16.61	0.95	0.80
T2	0.91	0.89	1.74	2.29	0.97	0.96
Rib 2 (R)	0.85	0.73	6.84	26.25	0.94	0.85
Rib 2 (L)	0.88	0.72	4.79	24.06	0.97	0.85
T3	0.90	0.89	2.24	2.32	0.96	0.96

Abbreviations: L left, R right, TS TotalSegmentator, tol. Tolerance.

distance of 3.4 mm versus 8.7 mm for TotalSegmentator and 2.0 mm inter-observer variability.

3.2.2. Performance of biomechanical registration

The build-up of biomechanical skeleton model can be performed with a subset of bones in the head and neck area, but biomechanical registration requires all bones listed in Table 1. Since the TotalSegmentator does not segment the skull, mandible, hyoid bone, and sternum, it cannot be used for biomechanical registration. For manual and nnU-Net-predicted labels the biomechanical registration is tested on three patients with each six fraction CT scans. The distance between landmarks (TRE) is summarised in Figure 5 for each patient and fraction CT. Median TRE is 1.44 ± 0.25 mm using manual segmentations and 1.51 ± 0.26 mm using nnU-Net segmentations. No significant difference in accuracy is observed among patients. The TRE distributions are similar for both methods, with no clear trend in registration quality throughout the treatment. Before deformable image registration, the median TRE ranges from 3.4 to 6.6 mm.

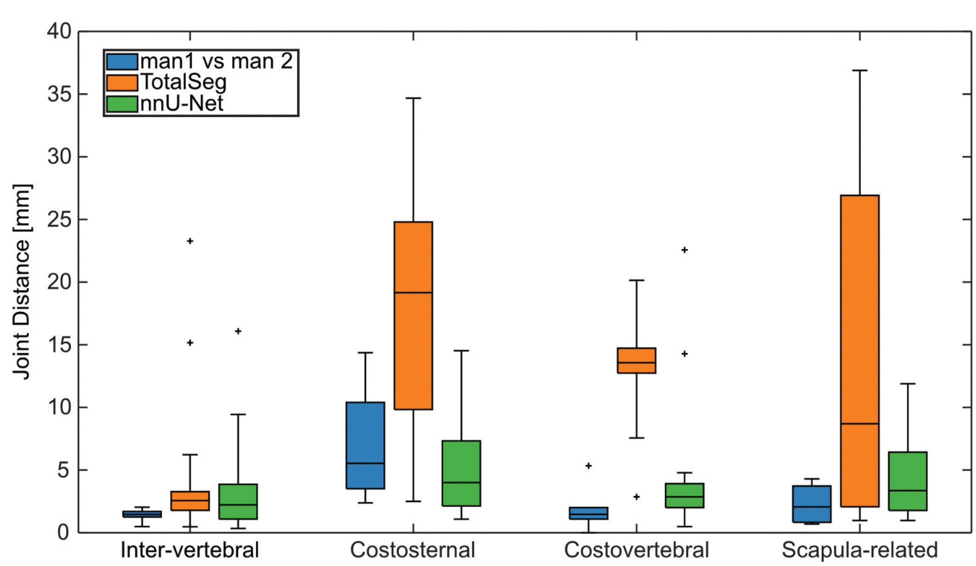

Figure 4. Boxplot of the distance in joint positioning between manual bone contours in comparison to a second set of manual contours (blue), the TotalSegmentator (ts)-generated contours (orange) and the custom-nnU-net-generated contours (green) grouped by joint types. Manual segmentations of two observers align well in their joint positioning (median distance ≤2 mm) for most joints on patient 15 reflecting inter-observer variability. The TotalSegmentator framework and the custom nnU-net cumulated over all three patients result in small joint position differences for the inter-vertebral joints, but larger distances for the other joint types.

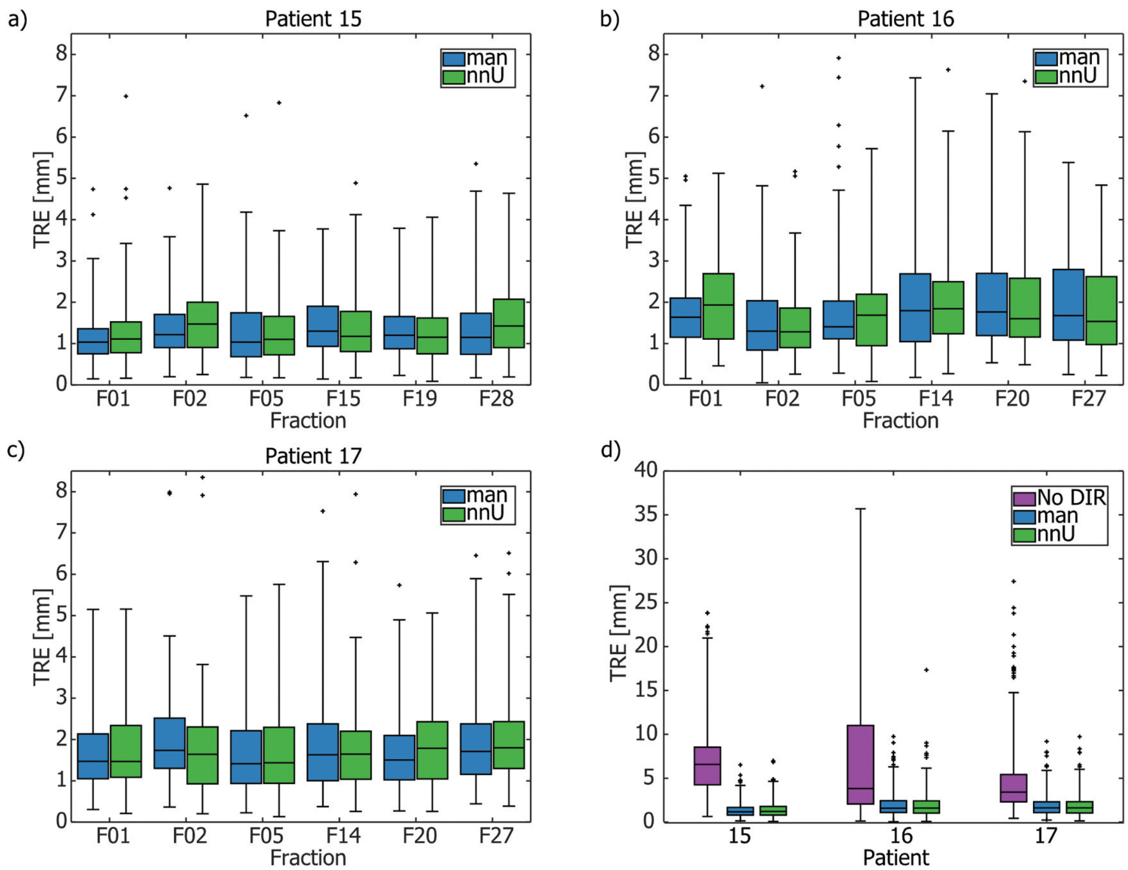

Figure 5. Boxplots of the distribution of the target registration error (TRE) after biomechanical registration for six fractions of patient 15–17 (a–c) manual segmentations (blue) and automatic segmentations by a custom trained nnU-net (green). (d) Summary plot indicating TRE distribution cumulated for all fractions per patient before registration (purple), with manual segmentation (blue), and automatic segmentations by a custom nnU-net (green).

4. Discussion

4.1. Accuracy of automatic segmentations

We analysed the biomechanical model build-up based on bone segmentations generated by a custom-trained nnU-Net model and the TotalSegmentator, an open-source pre-trained nnU-Net model. A 3D U-Net architecture for bone segmentation that is not based on the nnU-Net framework was investigated by Yawson et al. (2024) who found comparable segmentation accuracies for all bones if left and right instances were not confused. A postprocessing step allowed us to resolve this confusion (Yawson et al. 2024). For its public availability, we conducted this research using the nnU-Net and the TotalSegmentator.

In accordance with Maier-Hein et al. (2024), DICE, HD, and sDICE were chosen as evaluation metrics for the segmentation task (Maier-Hein et al. 2024). DICE and HD are often used together, combining volume-based and distance-based information. We chose sDICE as a second distance-based metric, reflecting changes at structure's surfaces, where most relevant changes of dose gradients appear. Comparing manual labels with predictions, all metrics showed that our custom-trained nnU-Net predictions aligned better than the TotalSegmentator predictions for most bones. The latter only showed slightly better alignment for C4, C5 and C6 in HD, and C5 in sDICE. Especially, for ribs and scapulae, our custom nnU-Net predictions aligned better with manual labels than TotalSegmentator predictions due to systematic deviations in the training labels and our on-purpose definition of the ribs including costal cartilage. With custom definitions, custom training intrinsically represents one's own data better but TotalSegmentator's extensive training on 1204 datasets could reasonably outweigh this advantage. Differences arose from the quality of bone labels in the training datasets. On their own dataset, the DICE values achieved using the TotalSegmentator by Wasserthal et al. (2022) exceeded the results achieved on our test dataset.

When compared to other custom-trained networks, the mean DICE between the manual labels and the predicted labels of individual bones on CT scans in this study were similar or better than previously published results (Buerger et al. 2020; Yip et al. 2014; Ibragimov and Xing 2017; Taghizadeh et al. 2019; Van der Veen et al. 2019; Van Dijk et al. 2020; Watkins et al. 2022), indicating the increasing advances of deep learning-based approaches and specifically the self-configuring nnU-Net framework as presented in Table 1.

4.2. Performance of the biomechanical model

Both models' automatic segmentations were sufficient for the automated build-up of the static skeleton model and joint positioning. While a DICE-based analysis showed comparable results, joint positioning varied considerably, implying the positioning of joints was sensitive to small changes in the segmentation. As a baseline, the median distance for overall joint positioning between two observers was less than 2 mm. Only the costosternal joints showed more than 5 mm distance cause by nearest- neighbour positioning strategy and the wide range of slices where the costal cartilage and sternum are closely connected.

When considering the impact of automatic segmentations on the joint positioning, the largest deviation was also seen for joints that are positioned using a nearest-neighbour approach. These joints were impacted by small inaccuracies at the surface of the segmentation. Deviations could be seen in the scapula region and the costosternal joints. Due to the relative stiffness of the rib cage and immobilisation techniques in radiotherapy, this did not affect the quality of the biomechanical registration result.

Intervertebral joints that are crucial for the articulation of the motion did not deviate significantly in the automatic segmentations. Since the presented biomechanical model positions inter-vertebral joint via the centre of mass of the vertebral bodies, the joint positioning was consistent between all segmentations and enabled accurate motion modelling in the registration task.

In contrast to our custom-trained nnU-Net model, the TotalSegmentator framework did not provide all required bones, so no registration was possible. The registration accuracy was therefore only analysed for the model build-up from nnU-Net predicted labels. For three patients (18 CT-CT pairs), the registration accuracy was equivalent to manual segmentations. The observed deviations in the positioning of joints had limited impact on the biomechanical registration and did not affect registration accuracy. For manual and automatic segmentation, the median TRE after registration was less than 0.5 mm above the median inter-observer variability indicating that the registration results were close to the best achievable accuracy. Thus, we showed that the labour-intensive manual segmentation process can be replaced by automatic segmentation for this head and neck biomechanical skeleton model in radiotherapy.

In a previous study, the biomechanical registration outperformed typical intensity-based approaches using B-splines using standard parameter settings and showed comparable results with the finest grid settings (Bauer et al. 2023). In combination, this underlines the competitive nature of biomechanical registration in the head and neck region based on automatic segmentations.

4.3. General comments

Although our custom-trained nnU-Net model outperformed TotalSegmentator predictions, it was trained on a limited amount of data which might seem restrictive. Other segmentation tasks showed that the nnU-Net framework also excels in challenges with small dataset sizes when compared to specialised models, for example, ranking first of 25 participants for a dataset of size 20 (heart dataset) [17, Supplementary Information]. This emphasises label quality over quantity. TotalSegmentator's systematic mislabelling of the ribs-vertebra-interface highlights training label quality issues.

Small datasets necessitate mirroring in data augmentation, causing frequent right-left misclassification. A rule-based algorithm successfully separated affected classes in our test set, but more complex post-processing may be needed for scans with larger slice thickness or smaller patient bodies.

5. Conclusion

We evaluated the capability of state-of-the-art deep-learning strategies to fully automate the contouring of individual bones in CT scans for motion simulation. Our study found that the application of a biomechanical skeleton model for image registration in the context of radiation therapy of the head and neck region is as accurate with deep-learning-generated contours as with manual ones. A custom nnU-Net, trained on self-curated data, provided the necessary quality of bone segmentations for automatic initialisation and model-based registration in adaptive radiotherapy workflows, even with a small number of labelled training cases.

The TotalSegmentator toolkit generally achieved similar segmentation quality but lacked the variety and specificities of bone segmentations needed to enable the articulated skeleton registration model, making it unsuitable for our biomechanical DIR.

Disclosure statement

No potential conflict of interest was reported by the author(s).

Funding

This study is funded by German Federal Ministry of Education and Research (BMBF) within the program "Bildgeführte Diagnostik und Therapie - Neue Wege in der Intervention" and the project ARTEMIS [13GW0436B]. AW is funded by the Helmholtz Information & Data Science School for Health (HIDSS4Health).

Notes on contributors

Alexandra Walter is a PhD student of the interdisciplinary graduate school HIDSS4Health, conducting research at the interface between Data Science and Health. The focus is on improving automatic segmentation algorithms needed in tumour therapy to calculate each individual radiation plan. Since 2023 she also conducts research in the field of model order reduction.

Cornelius J. Bauer is a researcher in the field of adaptive radiation therapy and computational image processing. In his work regarding biomechanical models, he investigates the potential of patient specific models in multimodal image registration and biofidelic generation of artificial data for the application in machine learning and data augmentation. With the combination of deformable image registration and deep learning–based techniques, he thrives to facilitate adaptive radiation therapy with photons and ions based on diverse imaging techniques.

Ama Katseena Yawson is a Software Scientist at the German Cancer Research Center.

Philipp Hoegen-Saßmannshausen is a Senior Physician at the Department of Radiation Oncology and Radiotherapy.

Sebastian Adeberg is the Director of the Department of Radiation Oncology of the University Hospital Marburg.

Jürgen Debus is the Chairman of the Executive Board of the Heidelberg University Hospital and Medical Director and Chairman of the Heidelberg University Hospital.

Oliver Jäkel is the Head of the Division Medical Physics in Radiation Oncology group at the German Cancer Research Center.

Martin Frank is the Director of the Scientific Computing Center (SCC) at KIT and Professor for Computational Science and Mathematical Methods in the Department of Mathematics at KIT.

Kristina Giske is the group leader of the Computational Patient Models group at the German Cancer Research Center.

Human subject research statements

This retrospective study was reviewed and approved by the Institutional Review Board of University Clinic Heidelberg (S-660/2022). The study was performed in accordance with the principles embodied in the Declaration of Helsinki and in accordance with the professional regulations of the State Medical Association of Baden-Württemberg.

References

Aguilera AR, Salas AL, Perandrés DM, Otaduy MA. 2015. A parallel resampling method for interactive deformation of volumetric models. Comp Graph. 53:147–155. doi: 10.1016/j.cag.2015.10.002.

Ang KK, Zhang Q, Rosenthal DI, Nguyen-Tan PF, Sherman EJ, Weber RS, Galvin JM, Bonner JA, Harris J, El-Naggar AK, et al. 2014. Randomized phase III trial of concurrent accelerated radiation plus cisplatin with or without cetuximab for stage III to IV head and neck carcinoma: RTOG 0522. J Clin Oncol. 32(27):2940. doi: 10.1200/JCO.2013.53.5633.

Arnold C, Biedebach L, Küpfer A, Neunhoeffer M. 2023. The role of hyperparameters in machine learning models and how to tune them. Political Sci Res Methods. 12(4):841–848.

Balakrishnan G, Zhao A, Sabuncu MR, Guttag J, Dalca AV. 2015. VoxelMorph: a learning framework for deformable medical image registration. IEEE Trans Med Imag. 38(8):1788–1800. doi: 10.1109/TMI.2019.2897538.

Bauer CJ, Teske H, Walter A, Hoegen P, Adeberg S, Debus J, Jäkel O, Giske K. 2023. Biofidelic image registration for head and neck region utilizing an in-silico articulated skeleton as a transformation model. Phys Med Biol. 68(9):095006. doi: 10.1088/1361-6560/acc7f1.

Bejarano T, De Ornelas-Couto M, Mihaylov IB. 2019. Longitudinal fan-beam computed tomography dataset for head-and-neck squamous cell carcinoma patients. Med Phys. 46(5):2526–2537. doi: 10.1002/mp.13460.

Bejarano T, De Ornelas-Couto M, Mihaylov IB. 2018. Head-and-neck squamous cell carcinoma patients with CT taken during pre-treatment, mid-treatment, and post-treatment dataset. Cancer Imag Archiv. doi: 10.7937/K9/TCIA.2018.13upr2xf.

Belal SL, Sadik M, Kaboteh R, Enqvist O, Ulén J, Poulsen MH, Trägårdh E, Høilund-Carlsen PF, Edenbrandt L, Trägårdh E. 2019. Deep learning for segmentation of 49 selected bones in CT scans: first step in automated pet/ct-based 3D quantification of skeletal metastases. Eur J Radiol. 113:89–95. doi: 10.1016/j.ejrad.2019.01.028.

Bendl R. 2006. Virtual therapy simulation. New technologies in radiation oncology 179–186. Berlin Heidelberg (NY): Springer Verlag.

Bergstra J, Bengio Y. 2012. Random search for hyper-parameter optimization. J Mach Learn Res. 13(2):281–305

Bosch WR, Straube WL, Matthews JW, Purdy JA. 2015. Data from head-neck_cetuximab. Cancer Imag Archiv. doi: 10.7937/K9/TCIA.2015.7AKGJUPZ.

Brock KK, Sharpe MB, Dawson LA, Kim SM, Jaffray DA. 2005. Accuracy of finite element model-based multi-organ deformable image registration. Med Phys. 32(6Part1):1647–1659. doi: 10.1118/1.1915012.

Buerger C, von Berg J, Franz A, Klinder T, Lorenz C, Lenga M. 2020. Combining deep learning and model-based segmentation for labeled spine CT segmentation. Med Imag Process. 11313:307–314. SPIE.

Campello VM, Gkontra P, Izquierdo C, Martin-Isla C, Sojoudi A, Full PM, Maier-Hein K, Zhang Y, He Z, Ma J, et al. 2021. Multi-centre, multi-vendor and multi-disease cardiac segmentation: the M&Ms challenge. IEEE Trans Med Imag. 40(12):3543–3554. doi: 10.1109/TMI.2021.3090082.

Clark K, Vendt B, Smith K, Freymann J, Kirby J, Koppel P, Moore S, Phillips S, Maffitt D, Pringle M, et al. 2013. The cancer imaging archive (TCIA): maintaining and operating a public information repository. J Digit Imag. 26(6):1045–1057. doi: 10.1007/s10278-013-9622-7.

Dice LR. 1945. Measures of the amount of ecologic association between species. Ecology. 26(3):297–302. doi: 10.2307/1932409.

Fu Y, Lei Y, Wang T, Curran WJ, Liu T, Yang X. 2023. Deep learning in medical image registration: a review. Phys Med Biol. 65(20):20TR01.

Giske K, Stoiber EM, Schwarz M, Stoll A, Muenter MW, Timke C, Roeder F, Debus J, Huber PE, Thieke C, et al. 2011. Jun 1. Local setup errors in image-guided radiotherapy for head and neck cancer patients immobilized with a custom-made device. Int J Radiat Oncol Biol Phys. 80(2):582–589. doi: 10.1016/j.ijrobp.2010.07.1980.

Ibragimov B, Xing L. 2017. Segmentation of organs-at-risks in head and neck CT images using convolutional neural networks. Med Phys. 44 (2):547–557. doi: 10.1002/mp.12045.

Isensee F, Jaeger PF, Kohl SA, Petersen J, Maier-Hein KH. 2021. nnU-net: a self-configuring method for deep learning-based biomedical image segmentation. Nat Methods. 18(2):203–211. doi: 10.1038/s41592-020-01008-z.

Kirby N, Chuang C, Pouliot J. 2011. A two-dimensional deformable phantom for quantitatively verifying deformation algorithms: a 2D phantom for verifying deformation algorithms. Med Phys. 38(8):4583–4586. doi: 10.1118/1.3597881.

Kiser K, Meheissen MAM, Mohamed ASR, Kamal M, Ng SP, Elhalawani H, Jethanandani A, He R, Ding Y, Rostom Y, et al. 2019. Prospective quantitative quality assurance and deformation estimation of MRI-CT image registration in simulation of head and neck radiotherapy patients. Clin Transl Radiat Oncol. 18:120–127. doi: 10.1016/j.ctro.2019.04.018.

Liu X, Song L, Liu S, Zhang Y. 2021. A review of deep-learning-based medical image segmentation methods. Sustainability. 13(3):1224. doi: 10.3390/su13031224.

Magadza T, Viriri S. 2021. Deep learning for brain tumor segmentation: a survey of state-of-the-art. J Imag. 7(2):19. doi: 10.3390/jimaging7020019.

Maier-Hein L, Reinke A, Godau P, Tizabi MD, Buettner F, Christodoulou E, Jäger PF, Isensee F, Kleesiek J, Kozubek M, Reyes M. 2024. Metrics reloaded: recommendations for image analysis validation. Nat Methods. 21(2):195–212. doi: 10.1038/s41592-023-02151-z.

Maurer CR, McCrory JJ, Fitzpatrick JM. 1993. Estimation of accuracy in localizing externally attached markers in multimodal volume head images. Med Imag 1993 Image Process. 1898:43–54). SPIE.

Nelder J, Mead R. 1965. A simplex method for function minimization. Comput J. 7(4):308. doi: 10.1093/comjnl/7.4.308.

Nikolov S, Blackwell S, Zverovitch A, Mendes R, Livne M, De Fauw J, Patel Y, Meyer C, Askham H, Romera-Paredes B, et al. 2021. Clinically applicable segmentation of head and neck anatomy for radiotherapy: deep learning algorithm development and validation study. J Med Internet Res. 23 (7):e26151. doi: 10.2196/26151.

Rockafellar RT, Wets RJB. 2009. Variational analysis Vol. 317. Berlin, Germany: Springer Science & Business Media.

Ronneberger O, Fischer P, Brox T. 2015. U-net: convolutional networks for biomedical image segmentation. In: Navab, N., Hornegger, J., Wells, W., Frangi, A. (eds), Medical image computing and computer-assisted intervention–MICCAI 2015: 18th international conference, Munich, Germany, October 5–9, 2015, proceedings Vol. Part III 18, Springer, Cham: Springer International Publishing; p. 234–241. doi:10.1007/978-3-319-24574-4_28.

Seth A, Sherman M, Eastman P, Delp S. 2010. Minimal formulation of joint motion for biomechanisms. Nonlinear Dyn. 62(1–2):291–303. doi: 10.1007/s11071-010-9717-3.

Sherman MA, Seth A, Delp SL. 2011. Simbody: multibody dynamics for biomedical research. Procedia IUTAM. 2:241–261. doi: 10.1016/j.piutam.2011.04.023.

Sørensen TA. 1948. A method of establishing groups of equal amplitude in plant sociology based on similarity of species content and its application to analyses of the vegetation on Danish commons. Biol Skar. 5:1–34.

Stergiopoulos V, Vassilakopoulos M, Tousidou E, Corral A. 2022. Hyper-parameters tuning of artificial neural networks: an application in the field of recommender systems. European Conference on Advances in Databases and Information Systems; Cham: Springer International Publishing. p. 266–276.

Stoiber EM, Bougatf N, Teske H, Bierstedt C, Oetzel D, Debus J, Bendl R, Giske K. 2017. Analyzing human decisions in IGRT of head-and-neck cancer patients to teach image registration algorithms what experts know. Radiat Oncol. 12(1):1–7. doi: 10.1186/s13014-017-0842-8.

Stoiber EM, Giske K, Schubert K, Sterzing F, Habl G, Uhl M, Herfarth K, Bendl R, Debus J. 2011. Local setup reproducibility of the spinal column when using intensity-modulated radiation therapy for craniospinal irradiation with patient in supine position. Int J Radiat Oncol* Biol* Phys. 81 (5):1552–1559. doi: 10.1016/j.ijrobp.2010.06.032.

Stoiber EM, Lechsel G, Giske K, Muenter MW, Hoess A, Bendl R, Debus J, Huber PE, Thieke C. 2009. Quantitative assessment of image-guided radiotherapy for paraspinal tumors. Int J Radiat Oncol* Biol* Phys. 75 (3):933–940. doi: 10.1016/j.ijrobp.2009.04.010.

Taghizadeh E, Terrier A, Becce F, Farron A, Büchler P. 2019. Automated CT bone segmentation using statistical shape modelling and local template matching. Computer methods in biomechanics and biomedical engineering. Comput Meth Biomech Biomed Eng. 22(16):1303–1310. doi: 10.1080/10255842.2019.1661391.

Teske H, Bartelheimer K, Bendl R, Stoiber EM, Giske K. 2017. Handling images of patient postures in arms up and arms down position using a biomechanical skeleton model. Curr Dir Biomed Eng. 3(2):469–472. doi: 10.1515/cdbme-2017-0099.

Teske H, Bartelheimer K, Meis J, Bendl R, Stoiber EM, Giske K. 2017. Construction of a biomechanical head and neck motion model as a guide to evaluation of deformable image registration. Phys Med Biol. 62(12):N271–N284. doi: 10.1088/1361-6560/aa69b6.

Vaassen F, Hazelaar C, Vaniqui A, Gooding M, van der Heyden B, Canters R, van Elmpt W. 2020. Evaluation of measures for assessing time-saving of automatic organ-at-risk segmentation in radiotherapy. Phys Imag Radiat Oncol. 13:1–6. doi: 10.1016/j.phro.2019.12.001.

Van der Veen J, Willems S, Deschuymer S, Robben D, Crijns W, Maes F, Nuyts S. 2019. Benefits of deep learning for delineation of organs at risk in head and neck cancer. Radiother Oncol. 138:68–74. doi: 10.1016/j.radonc.2019.05.010.

Van Dijk LV, Van den Bosch L, Aljabar P, Peressutti D, Both S, Steenbakkers RJ, Langendijk JA, Gooding MJ, Brouwer CL. 2020. Improving automatic delineation for head and neck organs at risk by deep learning contouring. Radiother Oncol. 142:115–123. doi: 10.1016/j.radonc.2019.09.022.

Wagenaar D, Kierkels RG, van der Schaaf A, Meijers A, Scandurra D, Sijtsema NM, Both S, Steenbakkers RJHM, Knopf AC, Langendijk JA, Both S. 2021. Head and neck IMPT probabilistic dose accumulation: feasibility of a 2 mm setup uncertainty setting. Radiother Oncol. 154:45–52. doi: 10.1016/j.radonc.2020.09.001.

Wasserthal J, Meyer M, Breit HC, Cyriac J, Yang S, Segeroth M, Heye T, Boll DT, Cyriac J, Yang S, et al. 2023. TotalSegmentator: robust segmentation of 104 anatomical structures in CT images. Radiol: Artif Intel. 5(5). doi: 10.1148/ryai.230024.

Watkins WT, Qing K, Han C, Hui S, Liu A. 2022. Auto-segmentation for total marrow irradiation. Front Oncol. 12:970425. doi: 10.3389/fonc.2022.970425.

Yawson AK, Walter A, Wolf N, Klüter S, Hoegen P, Adeberg S, Giske K, Frank M, Jäkel O, Giske K. 2024. Essential parameters needed for a U-Net-based segmentation of individual bones on planning CT images in the head and neck region using limited datasets for radiotherapy application. Phys Med Biol. 69(3):035008. doi: 10.1088/1361-6560/ad1996.

Yip S, Perk T, Jeraj R. 2014. Development and evaluation of an articulated registration algorithm for human skeleton registration. Phys Med Biol. 59 (6):1485. doi: 10.1088/0031-9155/59/6/1485.

Zou J, Gao B, Song Y, Qin J. 2022. A review of deep learning-based deformable medical image registration. Front Oncol. 12. doi: 10.3389/fonc.2022.1047215.

Zuley ML, Jarosz R, Kirk S, Lee Y, Colen R, Garcia K, Gur D, Sumkin JH. 2016. Breast MRI contrast enhancement kinetics of normal parenchyma correlate with presence of breast cancer. Breast Cancer Res BCR. 18(1). doi: 10.1186/s13058-016-0734-0.

Appendix

Table A1. Overview of patient data divided into training patients for the artificial neural network, and the test patients. For three of the test patients there also exist landmarks on sufficient fraction scans. Those patients are also used for accuracy evaluation of the deformable image registration. The table shows the diversity in treatment side, sex, age, CT scanner, acquisition parameters positioning set-up and availability of fraction imaging.

<table>
<tr><th colspan="2">Utilization</th><th>Pat ID</th><th>Treated for</th><th colspan="2">Sex | age</th><th>CT scanner | kVp | contrast agent</th><th colspan="3">CT (volume size | voxel size | setup)</th><th>Fraction imaging</th></tr>
<tr><td>Training</td><td></td><td>1</td><td>HNC</td><td>m</td><td>o</td><td>Siemens SOMATOM Dual Source | 120 kVp | contrast</td><td>512 × 198</td><td>0.98 × 2</td><td>Stereotact. frame, scotchcast mask, high head rest, vacuum mat, arms down</td><td>Siemens Primatom on-rails CT</td></tr>
<tr><td></td><td></td><td>2</td><td>HNC</td><td>f</td><td>o</td><td>TOSHIBA Aquilion | 120 kVp | contrast</td><td>512 × 125</td><td>0.98 × 3</td><td>-"-</td><td>Siemens Primatom on-rails CT</td></tr>
<tr><td></td><td></td><td>3</td><td>HNC</td><td>f</td><td>o</td><td>TOSHIBA Aquilion | 120 kVp | contrast</td><td>512 × 136</td><td>0.98 × 3</td><td>-"-</td><td>Siemens Primatom on-rails CT</td></tr>
<tr><td></td><td></td><td>4</td><td>HNC</td><td>f</td><td>40–50</td><td>Siemens Sensation Open | 120 kVp</td><td>512 × 116</td><td>0.98 × 3</td><td>thermoplastic mask, flat head rest, knee support, arms down</td><td>Elekta CBCTs</td></tr>
<tr><td></td><td></td><td>5</td><td>HNC</td><td>m</td><td>70–80</td><td>Siemens Sensation Open | 120 kVp</td><td>512 × 112</td><td>0.98 × 3</td><td>-"-</td><td>Elekta CBCTs</td></tr>
<tr><td></td><td></td><td>6</td><td>NeAx</td><td>o</td><td>10–20</td><td>Siemens Sensation Open | 120 kVp | pristine or native</td><td>512 × 124</td><td>0.98 × 2.6</td><td>-</td><td>Tomo MVCTs</td></tr>
<tr><td></td><td></td><td>7</td><td>ACC</td><td>o</td><td>40–50</td><td>Siemens SOMATOM Confidence | 120 kVp | native</td><td>512 × 109</td><td>0.98 × 3</td><td>thermoplastic mask, flat head rest, knee support, arms down, tooth filling removed</td><td>-</td></tr>
<tr><td></td><td></td><td>8</td><td>ACC</td><td>o</td><td>40–50</td><td>Siemens SOMATOM Confidence | 120 kVp | native</td><td>512 × 142</td><td>0.98 × 3</td><td>-"-</td><td>-</td></tr>
<tr><td></td><td></td><td>9</td><td>HNC</td><td>m</td><td>40–50</td><td>Siemens SOMATOM Confidence | 140 kVp | native</td><td>512 × 117</td><td>0.98 × 3</td><td>thermoplastic mask, MR-rot-capsule, arms down</td><td>Elekta CBCTs</td></tr>
<tr><td></td><td></td><td>10</td><td>HNC</td><td>f</td><td>50–60</td><td>Siemens SOMATOM Confidence | 140 kVp | native</td><td>512 × 123</td><td>0.98 × 3</td><td>-"-</td><td>Elekta CBCTs</td></tr>
<tr><td></td><td></td><td>11</td><td>WB</td><td>o</td><td>40–50</td><td>GE Systems Discovery STE | 120 kVp | 3 mAs</td><td>512 × 124</td><td>1.37 × 3.3</td><td>arms up</td><td>-</td></tr>
<tr><td></td><td></td><td>12</td><td>HNC</td><td>f</td><td>o</td><td>Philips Brilliance Big Bore | 120 kVp | 350mAs</td><td>512 × 112</td><td>0.98 × 3</td><td></td><td>-</td></tr>
<tr><td></td><td></td><td>13</td><td>WB</td><td>f</td><td>o</td><td>GE Systems Discovery STE | 120 kVp | 21 mAs</td><td>512 × 97</td><td>0.98 × 3.3</td><td>arms up</td><td>-</td></tr>
<tr><td></td><td></td><td>14</td><td>HNC</td><td>m</td><td>30–40</td><td>Siemens Sensation open | 120 kVp | 400 mAs</td><td>512 × 193</td><td>0.98 × 2</td><td></td><td>-</td></tr>
<tr><td>deep-learning-based contour evaluation</td><td>registration evaluation</td><td>15</td><td>HNC</td><td>m</td><td>o</td><td>TOSHIBA Aquilion | 120 kVp | contrast</td><td>512 × 124</td><td>0.98 × 3</td><td>stereotactic frame, scotchcast mask, high head rest, arms down</td><td>Siemens Primatom on-rails CT</td></tr>
<tr><td></td><td></td><td>16</td><td>HNC</td><td>m</td><td>o</td><td>TOSHIBA Aquilion | 120 kVp | contrast</td><td>512 ×155</td><td>0.98 × 3</td><td>-"-</td><td>Siemens Primatom on-rails CT</td></tr>
<tr><td></td><td></td><td>17</td><td>HNC</td><td>m</td><td>o</td><td>Siemens Somatom Dual Source | 120 kVp | contrast</td><td>512 ×135</td><td>0.98 × 2</td><td>-"-</td><td>Siemens Primatom on-rails CT</td></tr>
<tr><td></td><td></td><td>18</td><td>HNC</td><td>m</td><td>60–70</td><td>Siemens Sensation Open | 120 kVp</td><td>512 × 147</td><td>0.98 × 3</td><td>thermoplastic mask, flat head rest, knee support, arms down</td><td>Elekta CBCTs</td></tr>
<tr><td></td><td></td><td>19</td><td>HNC</td><td>m</td><td>50–60</td><td>Siemens Sensation Open | 120 kVp</td><td>512 × 145</td><td>0.98 × 3</td><td>thermoplastic mask, MR-rot-capsule, arms down</td><td>Elekta CBCTs</td></tr>
<tr><td></td><td></td><td>20</td><td>ACC</td><td>o</td><td>40–50</td><td>Siemens SOMATOM Confidence | 120 kVp | native</td><td>512 × 134</td><td>0.98 × 3</td><td>thermoplastic mask, flat head rest, knee support, arms down, tooth filling removed</td><td>-</td></tr>
<tr><td></td><td></td><td>21</td><td>HNC</td><td>m</td><td>50–60</td><td>Siemens SOMATOM Confidence | 140 kVp | native</td><td>512 × 139</td><td>0.98 × 3</td><td>-"-</td><td>Elekta CBCTs</td></tr>
<tr><td></td><td></td><td>22</td><td>HNC</td><td>m</td><td>50–60</td><td>Siemens SOMATOM Confidence | 140 kVp | native</td><td>512 × 142</td><td>0.98 × 3</td><td>-"-</td><td>Elekta CBCTs</td></tr>
</table>

Abbreviations: HNC head and neck cancer, NeAx neuroaxis, ACC adenocystic carcinoma, WB whole body, o anonymised, CBCT cone beam CT, MVCT megavoltage CT